

Cite this: *Nanoscale Adv.*, 2024, 6, 960

# Eco-friendly and sustainable basil seed hydrogel-loaded copper hydroxide-based catalyst for the synthesis of propargylamines and tetrazoles†

Effat Samiee Paghaleh,<sup>a</sup> Eskandar Kolvari,<sup>\*a</sup> Farzad Seidi<sup>id</sup><sup>b</sup> and Kheibar Dashtian<sup>id</sup><sup>c</sup>

The broad use of propargyl amines and tetrazoles in pharmaceutical applications presents a well-established challenge. Their synthesis relies heavily on catalysis, which, in turn, has been hindered by the scarcity of stable and practical catalysts. In response to this issue, we have developed an environmentally friendly and sustainable catalyst by infusing copper hydroxide into basil seed hydrogel (Cu(OH)<sub>2</sub>-BSH), creating a 3D nanoreactor support structure. To verify the structural, physical, chemical, and morphological properties of the prepared samples, a comprehensive analysis using various techniques, including FT-IR, EDX, FE-SEM, TEM, XRD, BET, TGA, and XPS, were conducted. The results not only confirmed the presence of Cu(OH)<sub>2</sub> but also revealed a porous structure, facilitating faster diffusion and providing a substantial number of active sites. This catalyst boasts a high surface area and can be easily recovered, making it a cost-effective, safe, and readily available option. This catalyst was applied to the synthesis of propargyl amines and tetrazoles through multi-component reactions (MCRs), achieving excellent results under mild conditions and in a remarkably short timeframe. Consequently, this work offers a straightforward and practical approach for designing and synthesizing metal hydroxides and 3D hydrogels for use in heterogeneous catalysis during organic syntheses. This can be achieved using basic and affordable starting materials at the molecular level.

Received 6th December 2023  
Accepted 11th January 2024

DOI: 10.1039/d3na01085f

rsc.li/nanoscale-advances

## 1. Introduction

Propargylamines and tetrazoles are versatile heterocyclic compounds widely utilized in medicine and industry. Propargylamines, distinguished by the presence of a carbon-carbon triple bond and a nitrogen atom, have been extensively leveraged in organic synthesis to access diverse heterocycles.<sup>1</sup> Notably, derivatives like rasagiline and selegiline find direct applications in treating neurodegenerative diseases.<sup>2</sup> The common production method for propargylamines involves alkylation processes, specifically the amination of propargylic halides, phosphates, or triflates.<sup>3</sup> Among various improved preparation methods, the A<sup>3</sup> coupling method stands out as the most efficient and direct approach. Tetrazoles, a distinct type of heterocyclic compounds, are doubly unsaturated aromatic heterocycles with a five-membered ring structure composed of one carbon atom and four nitrogen atoms.<sup>4</sup> Tetrazole

derivatives exhibit intriguing pharmacological properties and diverse biological activities, including anticonvulsant, anti-angiogenic, and anticancer effects.<sup>5-7</sup> While various synthetic approaches for 1,5-disubstituted and monosubstituted tetrazoles have been reviewed, the cyclization of nitriles and azide emerges as the most efficient method for tetrazole preparation.<sup>8</sup> Despite the advantages of these procedures, limitations such as extended reaction periods, the use of hazardous reagents, challenges in catalyst retrieval, and low yields need consideration. Therefore, there is a demand for advancing a straightforward and ecologically friendly approach to synthesizing propargylamines and tetrazoles. In this pursuit, careful catalyst selection and the adoption of an environmentally friendly approach are imperative. Recommendations for enhancing energy efficiency and achieving improved economic outcomes include the utilization of nanocatalysts aligned with the principles of green chemistry.<sup>9,10</sup> In the domain of catalytic techniques, homogeneous catalysts demonstrate commendable efficacy in terms of reactivity and selectivity. However, challenges related to their retrieval and elimination during the separation phase have spurred the adoption of heterogeneous catalysts, which possess active catalytic properties. The development of heterogeneous catalytic systems stands as a valuable strategy in organic transformations.<sup>11</sup> Notable catalysts applied in multicomponent reactions include copper supported on hydromagnesite (Cu/HM),<sup>12</sup> Ag-Cu-Ni immobilized on g-C<sub>3</sub>N<sub>4</sub>

<sup>a</sup>Department of Chemistry, Semnan University, P. O. Box 35131-19111, Semnan, Iran. E-mail: kolvari@semnan.ac.ir

<sup>b</sup>Jiangsu Co-Innovation Center of Efficient Processing and Utilization of Forest Resources and International Innovation Center for Forest Chemicals and Materials, Nanjing Forestry University, Nanjing 210037, China

<sup>c</sup>Department of Chemistry, Iran University of Science and Technology, Tehran, 16846-13114, Iran

† Electronic supplementary information (ESI) available. See DOI: <https://doi.org/10.1039/d3na01085f>



( $g\text{-C}_3\text{N}_4\text{-Ag-Cu-Ni}$ ),<sup>13</sup> and Au immobilized on the nitrogen porous triazine-based covalent organic polymer (Au-NCs@triazineCOP).<sup>14</sup> Metal hydroxides, another category of catalysts, exhibit diverse functional properties such as redox behavior, photocatalytic, and even piezoelectric properties.<sup>15</sup> From an economic perspective, methods for synthesizing metal hydroxides are cost-effective without the need for calcination.<sup>16</sup> Despite their notable catalytic characteristics, the application of metal hydroxides is hindered by challenges associated with aggregation. When particles are reduced to nano-sized dimensions, their surface energy increases, leading to the emergence of strong attraction forces, making these systems inherently unstable.<sup>17</sup> Metal hydroxides tend to undergo agglomeration to reduce the energy associated with their large surface areas. Unfortunately, this undesirable phenomenon significantly impairs the catalytic activity of metal hydroxides. Numerous studies have proposed elegant strategies to overcome this drawback, with the immobilization of metal hydroxides on solid supports emerging as one of the most reliable methods.<sup>18,19</sup> Solid supports used for this purpose are generally engineered from inorganic, organic, or hybrid materials.<sup>20,21</sup> The immobilization of metal hydroxides on biocompatible supports stands out as one of the most effective methods to enhance the efficiency, recovery, and sustainability of catalysts.<sup>22–25</sup>

Recently, polysaccharides have gained attention as supports for nanoparticles, leveraging their appealing attributes such as biodegradability, cost-effectiveness, and environmental friendliness.<sup>26–28</sup> Among polysaccharides, hydrogels stand out as a noteworthy class—highly hydrophilic three-dimensional, cross-linked networks formed through physical or chemical processes.<sup>29–32</sup> These hydrogels exhibit varying consistencies and toughness, characterized by cross-links with an exceptional affinity for water.<sup>30,33,34</sup> Notably, their porous structure, high surface area, capacity to accommodate diverse nano/microparticles, and potential for functionalization position hydrogels as a focal point in research for various applications.<sup>31,35,36</sup> Hydrogels, specifically those composed of naturally occurring polymers, fall under the category of natural hydrogels and can be classified into several types: (i) polysaccharides (*e.g.*, alginate), (ii) biological polymers (*e.g.*, nucleic acid), (iii) polyamides (*e.g.*, collagen), (iv) polyphenols (*e.g.*, lignin), (v) organic polyesters, (vi) inorganic polyesters (*e.g.*, polyphosphazene), and (vii) polyanhydrides (*e.g.*, poly sebacic acid). Hydrogels derived from natural polymers, particularly polysaccharides and proteins, inherently possess biocompatibility and are easily recognized by cells.<sup>37</sup> A notable example of a natural porous polysaccharide-based hydrogel is basil seed hydrogel, distinguished by its unique properties. This hydrogel serves as an excellent polymeric backbone for coordinating metal ions, thanks to the functional groups present in its structure. The basil seed biopolymer, characterized by broad chemical modification capacity and a high surface area, emerges as an intriguing biodegradable polymer suitable for supporting metal hydroxide catalysts.<sup>31,32</sup>

In this study, we successfully developed an eco-friendly and sustainable catalyst by incorporating copper hydroxide into basil seed hydrogel ( $\text{Cu}(\text{OH})_2\text{-BSH}$ ), establishing a 3D

nanoreactor support structure. A thorough analysis employing various techniques was conducted to verify the structural, physical, chemical, and morphological properties of the prepared samples. The findings not only confirmed the presence of  $\text{Cu}(\text{OH})_2$  but also unveiled a porous structure, facilitating rapid diffusion and offering a significant number of active sites. This catalyst exhibits a substantial surface area and can be easily recovered, rendering it a cost-effective, safe, and readily available option. Furthermore, when applied in the synthesis of propargyl amines and tetrazoles through multi-component reactions (MCRs), the catalyst demonstrated exceptional performance under mild conditions and within a remarkably short timeframe.

## 2. Experimental

### 2.1. Materials

Basil seeds were bought from a local market in Semnan, Iran. Copper chloride dihydrate ( $\text{CuCl}_2 \cdot 2\text{H}_2\text{O}$ ), sodium hydroxide ( $\text{NaOH}$ ), and other chemical substances and solvents were purchased from Merck Germany.

### 2.2. Instrumentation

The catalyst made investigated by FT-IR (Fourier transform infrared, Shimadzu 8400 S FT-IR spectrometer) spectrum of all samples was obtained using KBr disks. TGA was assessed in a thermogravimetric Linseis PT1000 from 30 to 800 °C under an  $\text{N}_2$  atmosphere at a heating rate of 10 °C  $\text{min}^{-1}$ . X-ray diffraction (XRD) patterns were performed on a Philips using a  $\text{CuK}\alpha$  radiation source. Scanning electron microscopy (SEM) FESEM-EDS images were collected using a TESCAN MIRA3 electron microscope. The Raman spectrum of the sample was determined by using a Raman spectrograph (LabRAM HR Evolution, Horiba, France). Transmission electron microscopy (TEM) images were received on a TEM Philips EM 208 S, and the microstructure of the samples was observed by the transmission electron microscopy model HR-TEM, JEM-2100 UHR, JEOL, Japan. For X-ray photoelectron spectroscopy (XPS), the AXIS UltraDLD spectrometer (Kratos, UK) with an  $\text{Al-K}\alpha$  X-ray source was used to analyze the data. Nitrogen adsorption-desorption isotherms were obtained by (Belsorp mini II, Japan) instrument.

### 2.3. $\text{Cu}(\text{OH})_2\text{-BSH}$ catalyst preparation

To prepare basil seed hydrogel, the process began by soaking purchased basil seeds in ethanol for 15 min. Subsequently, the mixture was filtered using filter paper and then dried in an oven at 50 °C for 24 h. Next, 0.3 g of the dried basil seeds were taken and soaked in 30 mL of deionized water for 60 minutes. Afterward, they were separated using filter paper. In the next step, the swollen basil seeds were immersed in a 0.4 M  $\text{NaOH}$  solution for 30 minutes to activate the hydroxyl groups of xylose within the basil seed hydrogel structure. Following this activation process, the treated basil seeds were separated using filter paper and rinsed three times with deionized water to remove any excess  $\text{NaOH}$ . To facilitate the chelation of  $\text{Cu}(\text{II})$  with the



basil seed hydrogel structure, 0.027 g of  $\text{CuCl}_2$  was added to the activated, swollen basil seeds. This mixture was allowed to react for 12 h at room temperature, followed by filtration and oven drying at 50 °C.

#### 2.4 General procedure for the synthesis of propargylamines

In this procedure, the reaction was initiated by combining 0.5 mmol of an aromatic aldehyde, 0.6 mmol of morpholine, and 0.75 mmol of phenylacetylene with 60 mg of  $\text{Cu}(\text{OH})_2$ -BSH catalyst. The mixture was then subjected to subsequent solvent-free magnetic stirring at 100 °C. To monitor the progress of the reaction, thin-layer chromatography (TLC) was used. Once the reaction had concluded, the resulting product was diluted with hot ethanol. Subsequently, the catalyst was separated from the product using a simple decantation method. The filtrate products were then allowed to dry at room temperature.

#### 2.5 General procedure for the synthesis of tetrazoles

To carry out this process, we combined 0.5 mmol of an aromatic aldehyde, 0.5 mmol of malononitrile, 0.75 mmol of sodium azide, and 1 mL of *N*-dimethylformamide as the solvent. Also 10 mg of  $\text{Cu}(\text{OH})_2$ -BSH catalyst was added to the mixture and the resulting mixture was then heated to 100 °C and stirred magnetically. The progression of the reaction was monitored using TLC. Once the reaction was completed, 10 mL of 2 N HCl was introduced to the reaction vessel. Subsequently, the catalyst and the final product were separated through a simple filtration process. The resulting substance was then filtered and allowed to dry at room temperature.

### 3. Results and discussion

The composition of basil seed's polysaccharide structure involves a tetramer, with 15 : 12 : 9 : 7 ratios of xylose (Xyl), galacturonic acid (Gala), arabinose (Ara), and rhamnose (Rha).<sup>38</sup> When basil seeds come into contact with water, their outer layer absorbs water molecules, leading to swelling. Copper ions ( $\text{Cu}$ ) are captured within the mucilage layer of basil seeds due to interactions with the hydroxyl functional groups. Fig. 1 shows an illustrative representation of the step-by-step process for preparing the  $\text{Cu}(\text{OH})_2$ -BSH catalyst. Additionally, the spectral data for propargylamine derivatives and tetrazole derivatives products are extensively detailed in Section S1 and S2, respectively.† The corresponding FTIR and HNMR results are depicted in Fig. S1 to S8†.

#### 3.1 Characterization of $\text{Cu}(\text{OH})_2$ -BSH catalyst

The structural (*e.g.*, FTIR, XRD, XPS), morphological (*e.g.*, SEM, TEM), inductively coupled plasma optical emission spectroscopy (ICP-OES), brunauer–emmett–teller analysis (BET), energy-dispersive X-ray spectroscopy (EDS), elemental mapping, and thermal analyses (*e.g.*, TGA) characterizations were applied for a full investigation of the physicochemical properties of raw basil seed and  $\text{Cu}(\text{OH})_2$ -BSH.

XRD analysis was conducted to examine the crystalline structure of both the basil seed hydrogel and the  $\text{Cu}(\text{OH})_2$ -BSH catalyst, as depicted in Fig. 2. Since the basil seed hydrogel is a naturally occurring polymer, it exhibits an amorphous structure, which is evident from its XRD pattern, which displays a prominent peak at  $2\theta$  ranging from 15° to 30° (Fig. 2a). On the

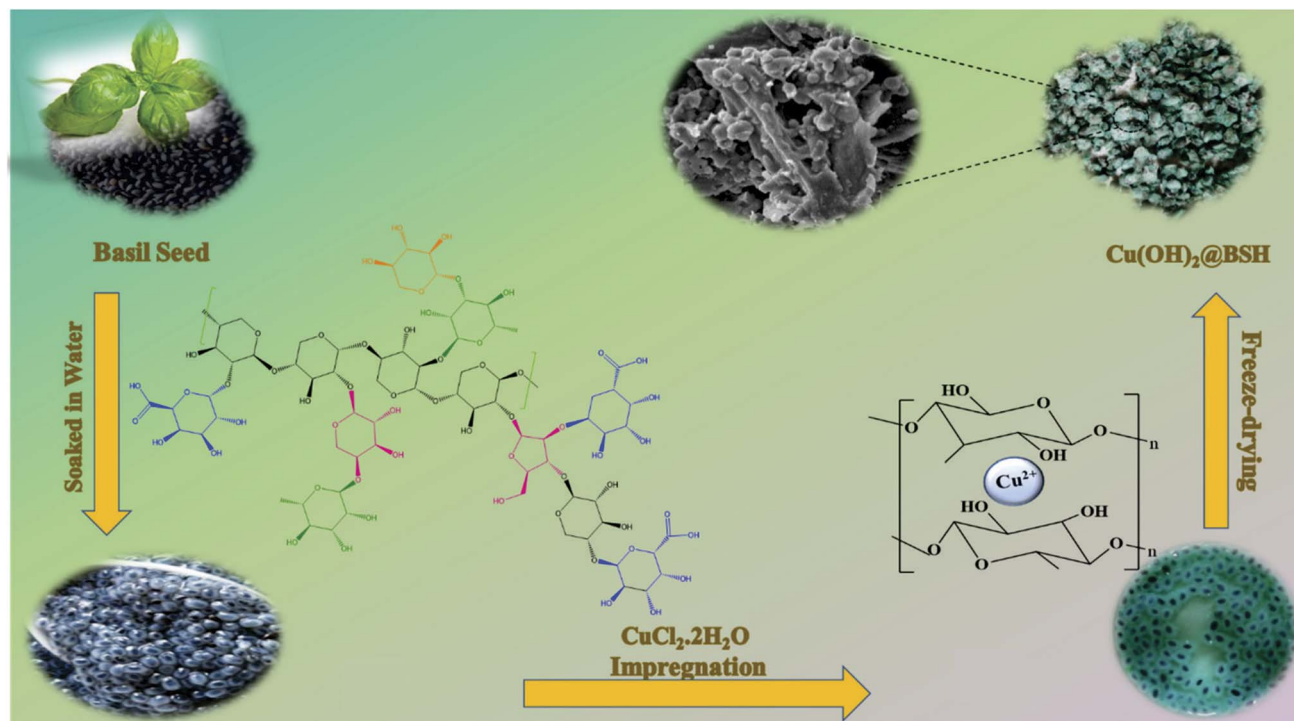


Fig. 1 Schematic representation of preparation steps for  $\text{Cu}(\text{OH})_2$ -BSH.



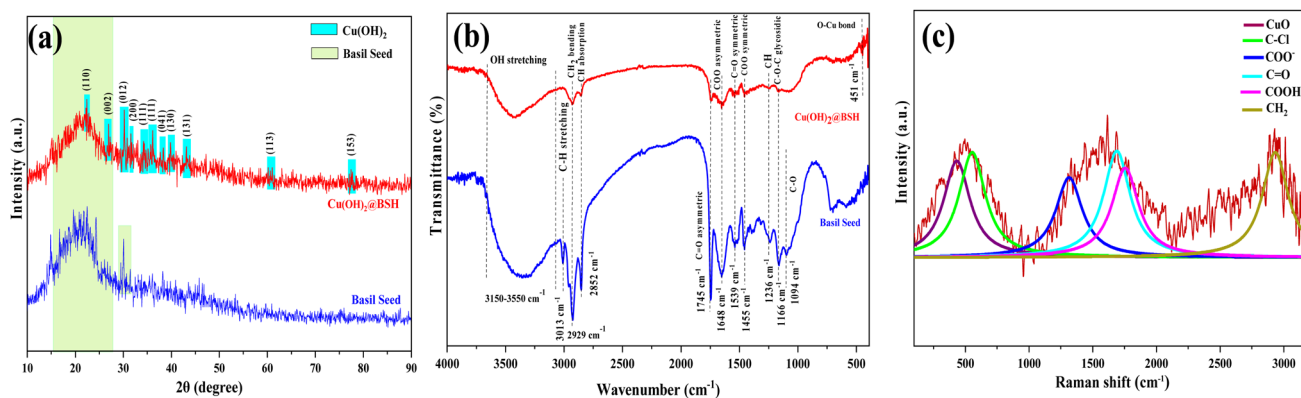


Fig. 2 XRD patterns (a), FT-IR spectra (b) and Raman spectra (c) of prepared samples.

other hand, the XRD pattern for  $\text{Cu}(\text{OH})_2\text{-BSH}$  (Fig. 2b) exhibits Bragg's diffraction peaks at  $2\theta$  values of  $22^\circ$ ,  $26.8^\circ$ ,  $30^\circ$ ,  $31.8^\circ$ ,  $35.6^\circ$ ,  $38^\circ$ ,  $39^\circ$ ,  $43.2^\circ$ ,  $61.3^\circ$ , and  $77.5^\circ$ . These peaks correspond to crystallographic planes (110), (002), (012), (200), (111), (041), (130), (131), (113), and (153), respectively. These reflections align with the JCPDS No. 013-0420 and 042-0638 standards associated with  $\text{Cu}(\text{OH})_2$ .<sup>39</sup>

Fig. 2b displays the FT-IR spectra of both the basil seed hydrogel substrate and  $\text{Cu}(\text{OH})_2\text{-BSH}$ , aiding in the identification of their respective functional groups. This investigation confirms the effective synthesis of the  $\text{Cu}(\text{OH})_2\text{-BSH}$  catalyst and its gradual modification. In the FT-IR spectrum of basil seed, various characteristic bands are observed, including those at  $1090\text{ cm}^{-1}$  (attributed to C–O stretching mode),  $1160\text{ cm}^{-1}$  (related to C–O–C stretching mode, indicating the stretching vibrations of polysaccharide glycosidic linkage), and  $1240\text{ cm}^{-1}$  (representing C–H stretching vibrational modes).<sup>40</sup> Bands at  $1460\text{ cm}^{-1}$  and  $1650\text{ cm}^{-1}$  signify uronic acid residues in the basil seed (C–OO asymmetric and symmetric band stretching vibrations). Furthermore, there are two peaks at  $1542\text{ cm}^{-1}$  and  $1745\text{ cm}^{-1}$ , corresponding to the stretching vibrations of the C=O symmetric and asymmetric atoms.<sup>41</sup> Additional features include peaks at  $2855\text{ cm}^{-1}$  (C–H absorption),  $2929\text{ cm}^{-1}$  ( $\text{CH}_2$  bending vibrations), and  $3010\text{ cm}^{-1}$  (C–H stretching vibration), as well as a broad band in the range of  $3150\text{--}3550\text{ cm}^{-1}$ , signifying hydroxyl alcohol groups.<sup>42</sup> Comparing the FT-IR spectra of hydrogels before and after  $\text{Cu}^{2+}$  immobilization reveals that the immobilization of  $\text{Cu}^{2+}$  leads to changes in the intensity of certain absorption bands. These changes are attributed to the interaction between  $\text{Cu}^{2+}$  ions and hydroxyl groups. Notably, in the FT-IR spectra of  $\text{Cu}(\text{OH})_2\text{-BSH}$ , a new band appears in the  $454\text{ cm}^{-1}$  region, which is attributed to the incorporation of the Cu–O bond into the structure of the fabricated catalyst.<sup>38</sup> Bands at  $464.81\text{ cm}^{-1}$  and  $420.45\text{ cm}^{-1}$  are indicative of the IR active modes for  $\text{Cu}(\text{OH})_2$ .<sup>43</sup>

Raman spectroscopy, a suitable technique for investigating the interactions that lead to the formation of hybrid hydrogel-nanoparticle materials, focuses on analyzing the vibrational energy of molecules.<sup>44</sup> Based on the Raman spectra of  $\text{Cu}(\text{OH})_2\text{-BSH}$  (Fig. 2c), the vibrations of Cu–O bonds are responsible for

the signals within the range of  $150\text{--}450\text{ cm}^{-1}$ .<sup>45</sup> Additionally, the peaks at  $1315\text{ cm}^{-1}$ ,  $1680\text{ cm}^{-1}$ , and  $1740\text{ cm}^{-1}$  are associated with  $\text{COO}^-$ ,  $\text{C}=\text{O}^-$ , and  $\text{COOH}$  groups, respectively.<sup>46</sup> Furthermore, vibrations in the regions of  $2900\text{--}2940\text{ cm}^{-1}$  and  $3210\text{--}3250\text{ cm}^{-1}$  are linked to  $\text{CH}_2$  and OH group vibrations, respectively.

The XPS survey spectrum (Fig. 3) provides valuable insights into the elemental composition of the synthesized catalyst, confirming the presence of copper. In the XPS survey spectrum (Fig. 3a), carbon, oxygen, and copper elements were observed at binding energies of  $286\text{ eV}$ ,  $531\text{ eV}$ , and  $935\text{ eV}$ , respectively. Furthermore, the C 1s spectrum (Fig. 3b) was deconvoluted into four peaks representing C–C, C–OH, C–O–C/C=O, and COOH components at binding energies of  $284\text{ eV}$ ,  $286\text{ eV}$ ,  $287\text{ eV}$ , and  $288\text{ eV}$ , respectively. The O 1s spectrum displayed two peaks at  $532\text{ eV}$  and  $533\text{ eV}$ , attributed to oxygen in hydroxide groups and carbonate groups, while the peak at  $534\text{ eV}$  could be attributed to the adsorption of  $\text{H}_2\text{O}$  molecules on the active materials (Fig. 3c). In contrast, the O 1s spectrum for  $\text{Cu}(\text{OH})_2$  exhibited a major peak at  $532\text{ eV}$ , confirming the formation of carbonate groups in the prepared compound. In Fig. 3d, the binding energies of Cu  $2p_{3/2}$  at  $933\text{ eV}$  and Cu  $2p_{1/2}$  at  $954\text{ eV}$ , along with two accompanying satellite peaks at  $942\text{ eV}$  and  $963\text{ eV}$ , provide information about the chemical state of  $\text{Cu}^{2+}$  in  $\text{Cu}(\text{OH})_2$ .<sup>38</sup> In summary, by cross-referencing the JCPDS No. 013-0420 code in XRD and conducting a comparative XPS study of  $\text{CuO}$ ,  $\text{Cu}_2\text{O}$ , and  $\text{Cu}(\text{OH})_2$ , it becomes apparent that the O 1s spectrum exhibits a distinct and robust peak at  $529\text{ eV}$  for  $\text{CuO}$  and  $530\text{ eV}$  for  $\text{Cu}_2\text{O}$ . Moreover, the spectra of  $\text{Cu}_2\text{P}$  in  $\text{Cu}(\text{OH})_2$  reveal approximately four clearly distinguishable peaks, whereas in the spectrum of  $\text{Cu}_2\text{P}$  in  $\text{Cu}_2\text{O}$ , only two peaks are observed.<sup>47–52</sup> Based on the compelling evidence and the alignment of the identified peaks with  $\text{Cu}(\text{OH})_2$ , a definitive conclusion can be drawn that  $\text{Cu}(\text{OH})_2$  is present.

The surface morphology of both the  $\text{Cu}(\text{OH})_2\text{-BSH}$  samples was investigated using FE-SEM at various magnifications (Fig. 4). The images reveal a consistent distribution of uniform and smooth  $\text{Cu}(\text{OH})_2$  nanoparticles within the basil seed hydrogel support, permeating the particles through BSH layers (Fig. 4a–c). The average size of  $\text{Cu}(\text{OH})_2$  nanoparticles was



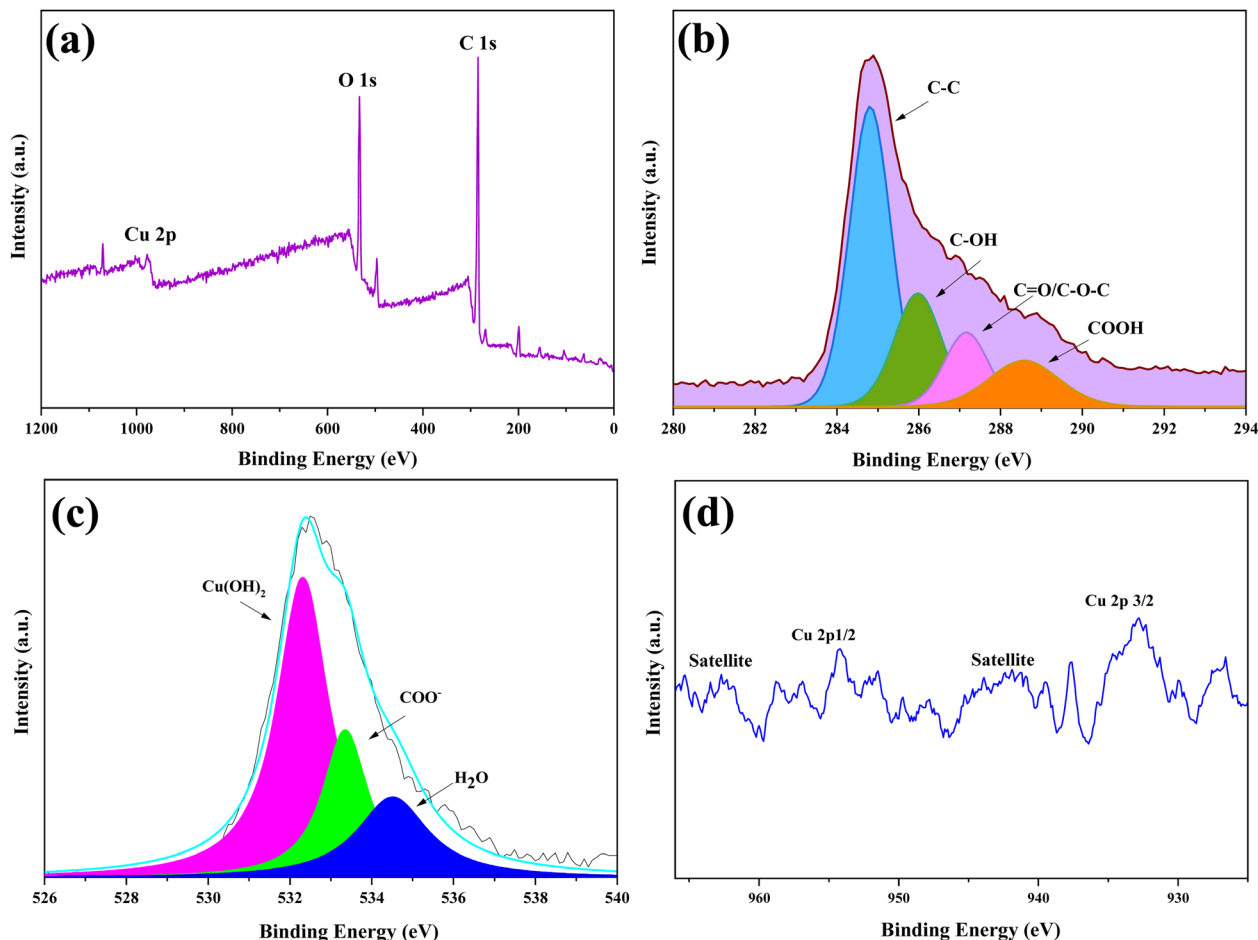


Fig. 3 XPS spectra of  $\text{Cu}(\text{OH})_2$ -BSH: survey (a), C 1s (b), O 1s (c), and Cu 2p (d).

estimated to be 23 nm. To gain a deeper understanding of the crystal structure of the  $\text{Cu}(\text{OH})_2$ -BSH nanocomposite and the visualized effects of self-assembly, high-resolution transmission electron microscopy (HR-TEM) analysis was employed (Fig. 4). HR-TEM images of the  $\text{Cu}(\text{OH})_2$ -BSH catalyst were captured at different magnifications to provide insights into the catalyst's structure. In Fig. 4d–f,  $\text{Cu}(\text{OH})_2$  nanoparticles (dark areas) are dispersed within the basil seed hydrogel substrate (gray areas). All of these particles, even the smallest ones, exhibit a crystal-line structure. This is evident in Fig. 4f, which shows a HR-TEM image with lattice plane distances of 0.208 nm, identifying the (111) facets of  $\text{Cu}(\text{OH})_2$ .<sup>53</sup>

Advanced chemical analytical techniques, including EDS analysis and elemental mapping, were employed to assess the atomic distribution, surface element concentration, and chemical composition of the prepared catalyst (Fig. 4g and h). The EDS spectra confirm the presence of Cu, C, O, S, P, and N elements in the catalyst. Additionally, the elemental mapping images demonstrate the successful anchoring of  $\text{Cu}(\text{OH})_2$  onto the basil seed hydrogel. The presence of S and P elements is observed in the natural basil seeds source. The ICP-OES analysis confirms the presence of 4.2% copper per 10 mg of the catalyst, whereas the recycled catalyst exhibits 2.7% copper in a 10 mg

sample. This supports the assertion of the prepared catalyst's desirable stability.

$\text{N}_2$  adsorption–desorption analysis was carried out at 77 K to evaluate the textural characteristics and porosity of the  $\text{Cu}(\text{OH})_2$ -BSH catalyst. Fig. 5a displays the corresponding nitrogen adsorption–desorption isotherm. According to the IUPAC classification, the mesoporous catalyst exhibits a type III isotherm (Fig. 5a) with H3-type hysteresis loops (Fig. 5b).<sup>54</sup> A closer examination of the hysteresis loop reveals that its end is open, suggesting the presence of microscopic pores on the catalyst's surface. Based on the results obtained from these analyses, the  $\text{Cu}(\text{OH})_2$ -BSH catalyst has a BET surface area of  $5.70 \text{ m}^2 \text{ g}^{-1}$ , a pore volume of  $0.0051 \text{ cm}^3 \text{ g}^{-1}$ , and an average pore diameter of 3.59 nm.<sup>55</sup> The thermal stability of both basil seed hydrogel and the  $\text{Cu}(\text{OH})_2$ -BSH catalyst was assessed using thermogravimetric analysis (TGA) and differential thermogravimetric analysis (DTG). Basil seed hydrogel exhibited four stages of thermal degradation, as depicted in Fig. 5a. The initial weight loss (6.1%) is attributed to moisture removal. The second stage of weight loss (44.7%) results from the breakdown of hemicellulose polysaccharides (such as xylan, glucomannan, etc.) and glycosidic linkages in cellulose. Weight loss in stages three (13.9%) and four (33%) is associated with the thermal



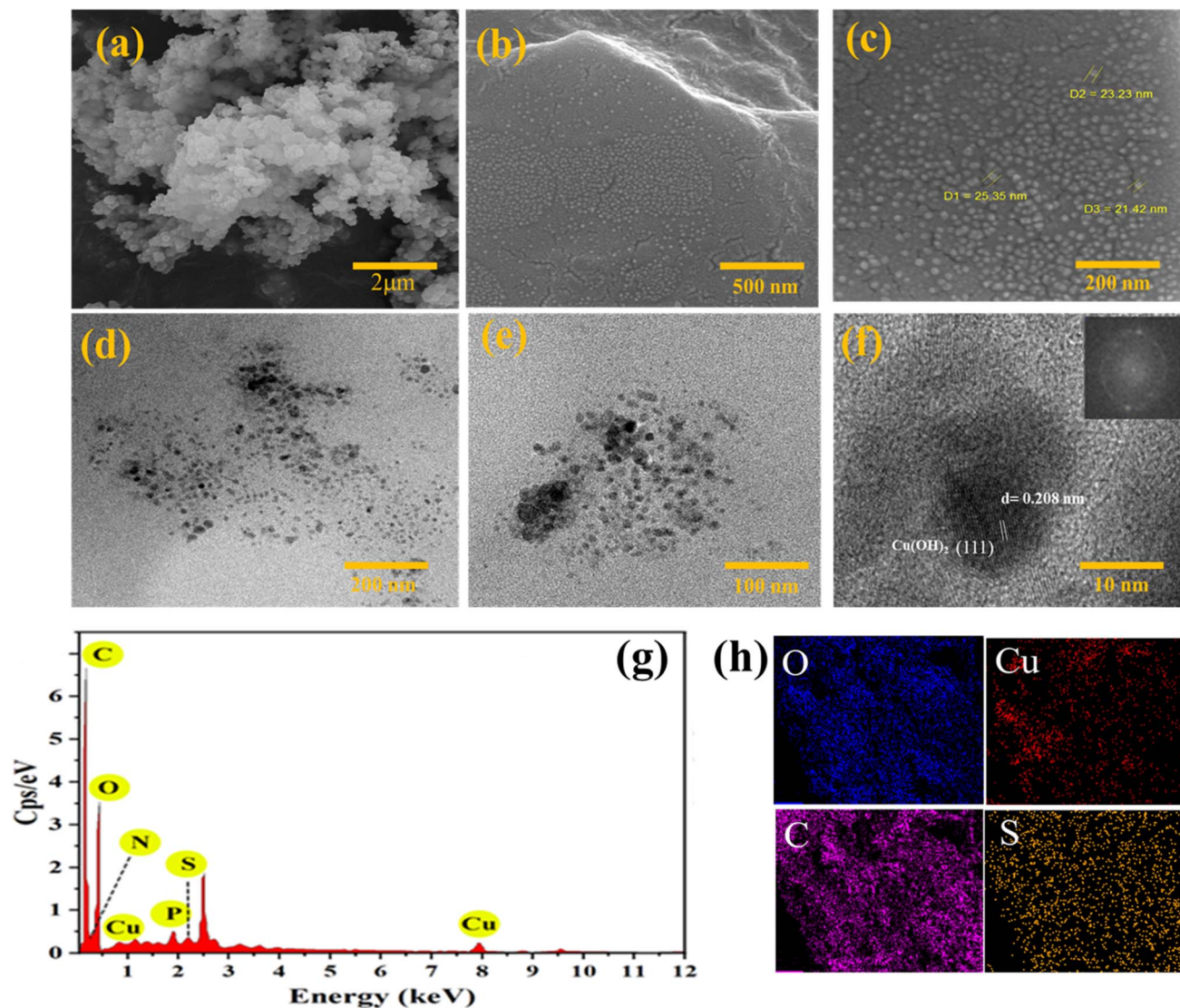


Fig. 4 FESEM images at different magnifications (a–c), TEM images at different magnifications (d–f), EDX spectra (g) and element mapping images of C, O, Cu, S (h) of  $\text{Cu}(\text{OH})_2$ -BSH.

decomposition of cellulose and lignin, respectively. Upon the incorporation of  $\text{Cu}(\text{OH})_2$  nanoparticles, the thermal behavior was slightly altered, and an increase in thermal stability was observed (Fig. 5b). This improvement in thermal stability can be attributed to the coordination of the hydroxyl and carboxyl groups of the basil seed hydrogel with  $\text{Cu}^{2+}$ . The inclusion of  $\text{Cu}(\text{OH})_2$  NPs enhanced the thermal stability of the basil seed hydrogel.

### 3.2. Swelling ratio measurement

The swelling ratio ( $R_s$ ) of a hydrogel is a measurable parameter that quantifies the increase in mass or volume of the hydrogel. It can be calculated using the formula  $R_s = ((W_s - W_d)/W_d) \times 100$ , where  $W_s$  represents the weight or volume of the swollen hydrogel and  $W_d$  represents the weight or volume of the dry (unswollen) hydrogel. In your provided information, the hydrogel swelling ratio was determined to be 1270 for the

swollen BSH hydrogel and 775 for the swollen BSH hydrogel in the presence of copper(II) chloride. This indicates that the presence of copper(II) chloride has a noticeable effect on the swelling behavior of the hydrogel, reducing the extent of swelling when compared to the hydrogel without the copper compound.

### 3.3. Catalytic activity

After successfully synthesizing and confirming the catalyst through various methods, the catalytic performance of  $\text{Cu}(\text{OH})_2$ -BSH was evaluated for the synthesis of propargylamines and tetrazoles *via*  $A^3$  coupling and cycloaddition reactions, respectively (Scheme 1).<sup>56</sup>

**3.3.1. The catalytic activity of  $\text{Cu}(\text{OH})_2$ -BSH in the  $A^3$  coupling reaction.** This was accomplished by utilizing the model reaction of benzaldehyde, morpholine, and phenylacetylene in the  $A^3$  coupling procedure, which involves the



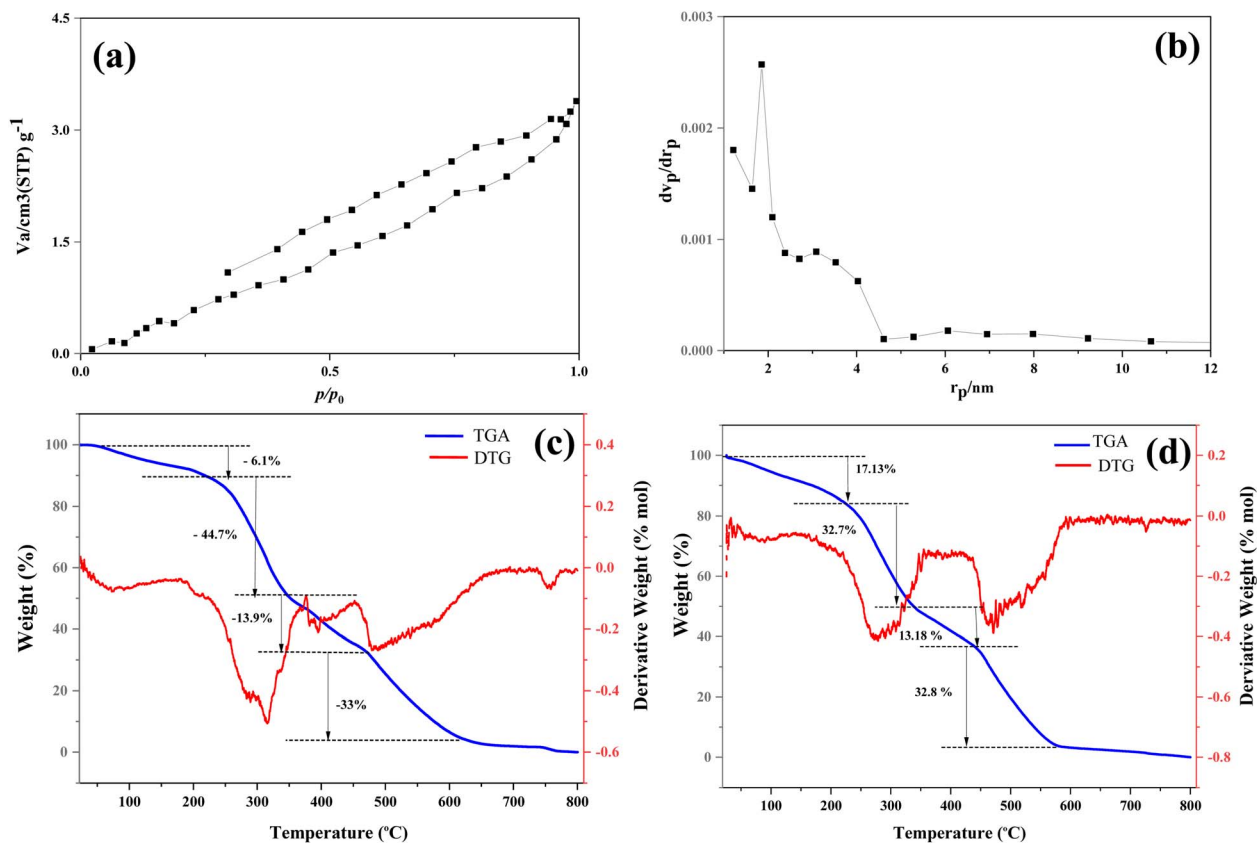
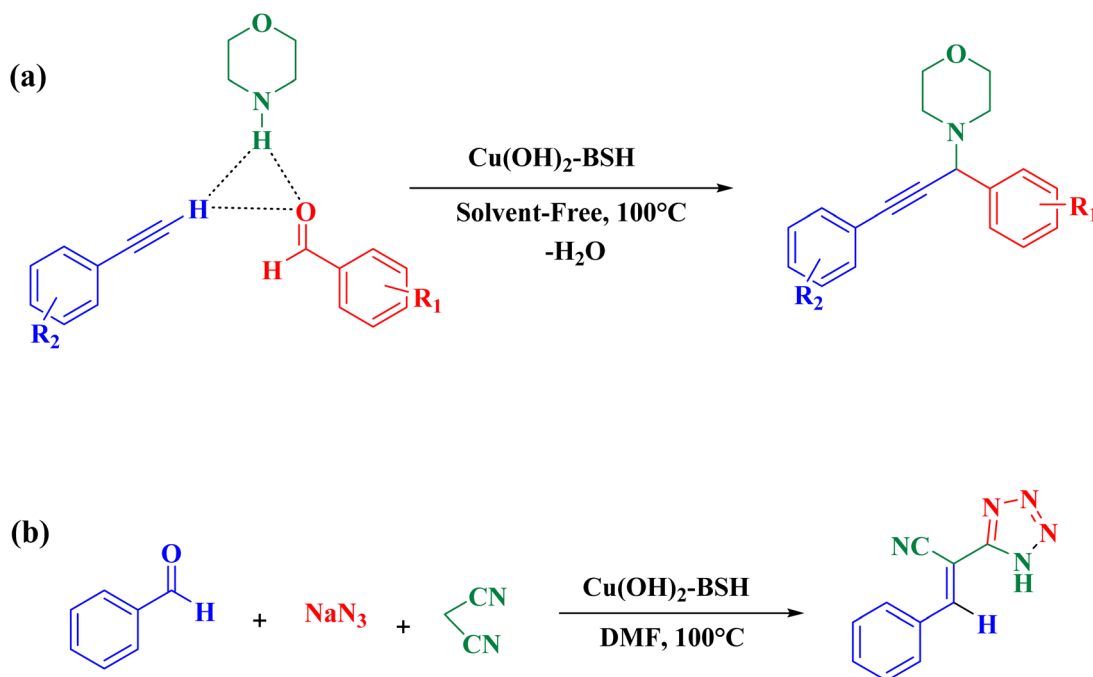


Fig. 5 (a)  $N_2$  adsorption/desorption, (b) pore size distribution of  $Cu(OH)_2$ -BSH and TGA-DTG of (c) BSH and (d)  $Cu(OH)_2$ -BSH samples.



Scheme 1 Synthesis of propargylamines and tetrazoles through (a)  $A^3$  coupling and (b) [3 + 2] cycloaddition reactions.

amount of catalyst, temperature, and solvent. At first, different amounts of the catalyst were used in the reaction, which was conducted at 100 °C under solvent-free conditions (Table 2,

entries 1–4). The results showed that the catalyst with the highest efficiency was 0.06 g and that increasing the catalyst concentration had no beneficial effect on the yield of the



Table 1 Optimization of A<sup>3</sup> coupling reaction conditions<sup>a</sup>

Entry	Amount of catalyst (g)	Solvent	Temperature (°C)	Time <sup>b</sup> (h:min)	Yield <sup>c</sup> (%)
1	0.03	—	100	00:30	50
2	0.05	—	100	00:30	60
3	0.06	—	100	00:30	100
4	0.07	—	100	00:30	60
5	0.06	—	R.T.	05:00	—
6	0.06	—	50	05:00	30
7	0.06	—	80	05:00	60
8	0.06	EtOH	100	02:00	50
9	0.06	EtOH · H <sub>2</sub> O	100	02:00	65
10	0.06	CH <sub>3</sub> CN	100	02:00	100
11 <sup>d</sup>	0.06	H <sub>2</sub> O	100	00:05	100
12 <sup>e</sup>	0.06	H <sub>2</sub> O	100	05:00	—

<sup>a</sup> Reaction conditions: benzaldehyde (0.5 mmol), morpholine (0.6 mmol), phenylacetylene (0.75 mmol), Cu(OH)<sub>2</sub>-BSH (0.06 g). <sup>b</sup> Detected by TLC.

<sup>c</sup> Isolated yield. <sup>d</sup> Benzaldehyde. <sup>e</sup> 4-Nitrobenzaldehyde.

reaction. Next, the effectiveness of temperature was evaluated by performing the same reaction at various temperatures (Table 1, entries 3, 5–7). For this process, a temperature of 100 °C was acceptable (Table 1, entry 3, 8–12). The sample reaction was then tested in a variety of solvents, including H<sub>2</sub>O, EtOH, H<sub>2</sub>O:EtOH, and CH<sub>3</sub>CN, as well as in solvent-free conditions, in order to find a suitable solvent (Table 1, entries 3, 8–12). These findings suggested that the most advantageous system was the solvent-free state (Table 1, entry 3). Thus, employing 0.06 g of Cu(OH)<sub>2</sub>-BSH catalyst and a reaction duration of 30 min, the optimal conditions were found at a temperature of 100 °C.

The Cu(OH)<sub>2</sub>-BSH catalyst was examined to make a variety of propargylamines after identifying the best reaction conditions, and the outcomes are described in Table 2. Numerous aldehydes interacted with morpholine, and under solvent-free conditions, 0.06 g of catalyst promoted the phenylacetylene reaction to produce the related A<sup>3</sup> products. Propargylamines were successfully produced in good to high yields by the efficient reaction of the aromatic aldehydes with morpholine and

phenylacetylene. Additionally, the electronic effect on the outcome of the reaction is remarkably effective for aromatic aldehydes; as a result, aromatic aldehydes with electron donor groups yield higher yields than aromatic aldehydes with electron receptor groups.

**3.3.2. The catalytic activity of Cu(OH)<sub>2</sub>-BSH in tetrazoles synthesis.** To achieve this, a model reaction including benzaldehyde, malononitrile, and sodium azide was utilized to optimize the reaction variables, which include the amount of catalyst, the amount of sodium azide, the temperature, and the solvent. The outcomes of the optimization conditions are summarized in Table 3. The model reaction was first tested at 100 °C in a DMF solvent with various catalyst concentrations. The results revealed that 0.01 g of the catalyst had the highest efficiency, and adding more catalyst had no positive effects on the reaction's yield (Table 4, entries 1–3). Next, the effectiveness of temperature was evaluated by performing the same reaction at various temperatures (Table 3, entries 2, 4, 5). For this reaction, a temperature of 100 °C was acceptable. The model reaction was then tested in a variety of solvents, including DMF, H<sub>2</sub>O, EtOH, and solvent-free conditions, in order to find a suitable solvent (Table 3, entries 2, 6–8). These findings suggested that the best solvents to use were DMF and water.

The investigation of Cu(OH)<sub>2</sub>-BSH to manufacture a variety of tetrazoles after establishing optimal reaction conditions yielded the results shown in Table 4. The position of the comparable groups on the aromatic ring played no notable influence on the outcome of the reaction, which was carried out in the presence of both benzaldehyde bearing electron-releasing and withdrawing functional groups on the aryl ring. At a pre-determined moment, every reaction was finished. High yields of the pure tetrazoles were isolated.

### 3.4. Reaction mechanism

Scheme 2a outlines a potential reaction mechanism for the one-pot, three-component A<sup>3</sup> coupling reaction that yields propargylamines in the presence of Cu(OH)<sub>2</sub>-BSH. Based on previous research,<sup>53</sup> the reaction is initiated by Cu(II) adsorbed on basil

Table 2 Synthesis of various propargylamines catalyzed by Cu(OH)<sub>2</sub>-BSH<sup>a</sup>

Entry	R <sub>1</sub>	Time (h:min)	Yield (%)
1	H	00:30	100
2	4-CH <sub>3</sub>	02:40	80
3	4-Cl	02:25	100
4	4-Br	04:30	100
5	3-Cl	03:45	90
6	4-NO <sub>2</sub>	05:00	10
7	3-NO <sub>2</sub>	04:30	30
8	2-OH	03:20	80
9	4-OMe	04:40	99
10	3-OEt-4-OH	06:00	80
11	4-N(CH <sub>3</sub> ) <sub>2</sub>	05:45	100
12	1,4-Diphenyl	12:12	95

<sup>a</sup> Reaction conditions: aryl aldehyde (0.5 mmol), morpholine (0.6 mmol), phenylacetylene (0.75 mmol), Cu(OH)<sub>2</sub>-BSH (0.06 g), solvent-free, 100 °C.



Table 3 Optimization of reaction conditions in the tetrazoles reaction synthesis<sup>a</sup>

Entry	Amount of catalyst (g)	Solvent	Temperature (°C)	Time <sup>b</sup> (h:min)	Yield <sup>c</sup> (%)
1	0.005	DMF	100	00:05	70
2	0.01	DMF	100	00:05	100
3	0.03	DMF	100	00:05	100
4	0.01	DMF	R.T.	00:05	40
5	0.01	DMF	50	00:05	60
6	0.01	—	100	01:00	60
7	0.01	EtOH	100	01:00	80
8	0.01	H <sub>2</sub> O	100	01:00	95

<sup>a</sup> Reaction conditions: benzaldehyde (0.5 mmol), malononitrile (0.5 mmol), sodium azide (0.75 mmol), Cu(OH)<sub>2</sub>-BSH (0.01 g). <sup>b</sup> Detected by TLC.

<sup>c</sup> Isolated yield.

Table 4 Synthesis of various tetrazoles catalyzed by Cu(OH)<sub>2</sub>-BSH<sup>a</sup>

Entry	R <sub>1</sub>	Solvent: DMF		Solvent: H <sub>2</sub> O	
		Time (min)	Yield (%)	Time (min)	Yield (%)
1	H	00:05	100	01:00	95
2	4-CH <sub>3</sub>	00:20	90	02:13	90
3	4-Cl	00:20	100	03:00	100
4	4-Br	01:00	90	02:20	90
5	4-NO <sub>2</sub>	00:05	100	02:00	100
6	3-NO <sub>2</sub>	00:05	100	02:32	95
7	2-OH	00:20	100	01:38	95
8	4-OH	00:15	100	00:10	100
9	3-OEt-4-OH	00:15	100	00:20	100
10	4-N(CH <sub>3</sub> ) <sub>2</sub>	00:10	100	00:20	100
11	1,4-Diphenyl	00:05	100	02:00	80

<sup>a</sup> Reaction conditions: aryl aldehyde (0.5 mmol), malononitrile (0.5 mmol), sodium azide (0.75 mmol), Cu(OH)<sub>2</sub>-BSH (0.01 g), 100 °C.

seed, which activates the terminal C–H bond of acetylene. This step is crucial in increasing the acidity of the terminal proton to facilitate its removal. On the surface of the composite, the reaction results in the formation of a copper alkylidene intermediate **B** and a metal-alkyne intermediate **A**. The catalyst may also promote the reaction between an aldehyde and a secondary amine, leading to the formation of iminium ions.<sup>3</sup> Furthermore, Scheme 2b illustrates a potential process for the synthesis of tetrazole derivatives. Arylidene malononitrile **A** is initially generated through the Knoevenagel condensation, where the carbonyl oxygen atom of the aromatic aldehyde interacts with the Cu(OH)<sub>2</sub>-BSH catalyst. The catalyst then combines with the nitrogen atom of this intermediate **A** to form complex **B**, rendering it more reactive for the attack of the azide ion. The cycloaddition between the azide ion and the CN group of arylidene malononitrile creates intermediate **C**. Finally, tetrazole derivatives are produced upon the addition of HCl.<sup>56</sup> In summary, the hydroxyl groups present on the substrate serve as active catalytic sites capable of activating carbonyl groups. However, their catalytic activity is limited to the intermediate step. The incorporation of copper into the hydrogel amplifies the activation of hydroxyl groups through an electron exchange between copper ions and hydroxyl groups. This results in the

formation of two distinct active sites on the substrate, one composed of copper and the other of hydroxyl. The electron exchange between these sites expedites the reaction.<sup>57</sup> Moreover, the presence of pores in the catalyst widens the dispersion of the active sites of copper hydroxide and improves the accessibility of the catalyst's active sites to reactive molecules. This, in turn, facilitates the ingress of organic substances into the pores and their interaction with the active sites.<sup>58</sup>

### 3.5. Catalyst stability and reusability

Catalyst recovery and reusability are crucial aspects of industrial sustainable chemistry and economic feasibility. We thoroughly examined the catalyst recovery during the synthesis of propargylamine and tetrazole to assess this potential. The process involved covering the catalyst with filter paper after the initial reaction run, isolating it, and then cleaning it meticulously with hot ethanol several times. Once cleaned, the catalyst was dried and reused for subsequent reaction runs. Fig. 6a and b illustrate that the catalyst could be recovered and reused at least four times for the synthesis of propargylamine and five times for the synthesis of tetrazole without a significant degradation in its catalytic efficiency.

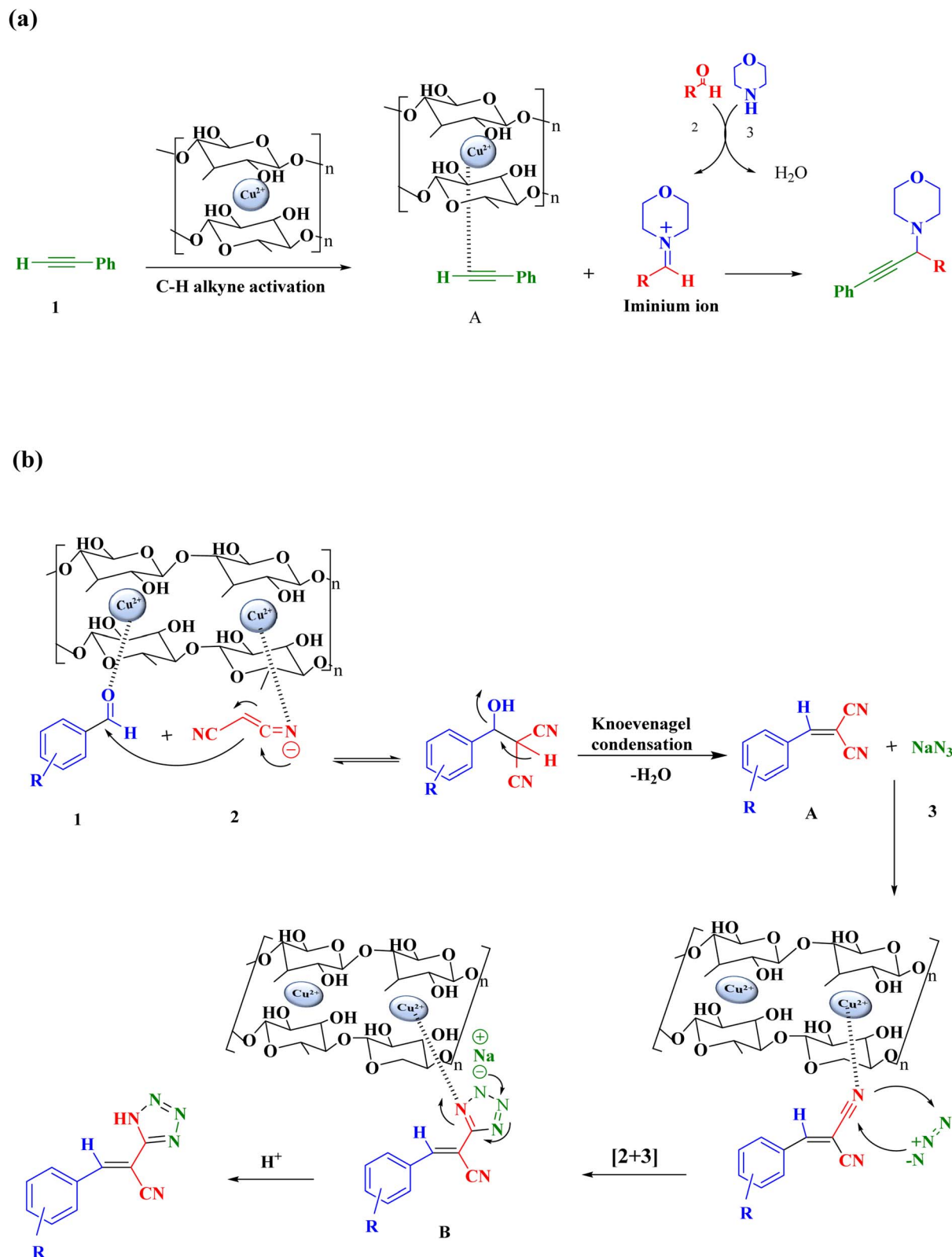
The heterogeneous nature of the catalyst was examined by extracting it from the reaction environment. In this experiment, the reaction was halted after 15 min (in this specific case), and the catalyst was thoroughly eliminated using filter paper before resuming the reaction. Interestingly, there was no discernible enhancement in the product yield after 15 min of reaction time without the catalyst (as monitored by TLC).

Including FT-IR spectra (Fig. 7a) and XRD pattern (Fig. 7b) along with digital photographs (Fig. 7c and d) of the fresh and reused Cu(OH)<sub>2</sub>-BSH catalyst offers a comprehensive analysis of the sample after the catalytic process. These results undeniably confirm the structural and morphological stability of the Cu(OH)<sub>2</sub>-BSH catalyst, thereby validating its practical applicability and reusability.

### 3.6. Comparison of the fabricated catalyst with other works

In Tables 5 and 6, which focus on propargylamine and tetrazole derivatives, respectively, we compare the catalytic performance of the Cu(OH)<sub>2</sub>-BSH catalyst with several other well-known





Scheme 2 A possible mechanism for the synthesis of (a) propargylamines and (b) tetrazoles in the presence of  $\text{Cu}(\text{OH})_2$ -BSH catalyst.

heterogeneous catalysts. The innovative catalyst is constructed using cost-effective and environmentally friendly components, with a basil seed nanoreactor containing  $\text{Cu}(\text{OH})_2$ , and it

exhibits remarkable stability, a straightforward synthesis process, and reusability. However, it's worth noting that the mentioned catalysts do offer certain advantages over others.

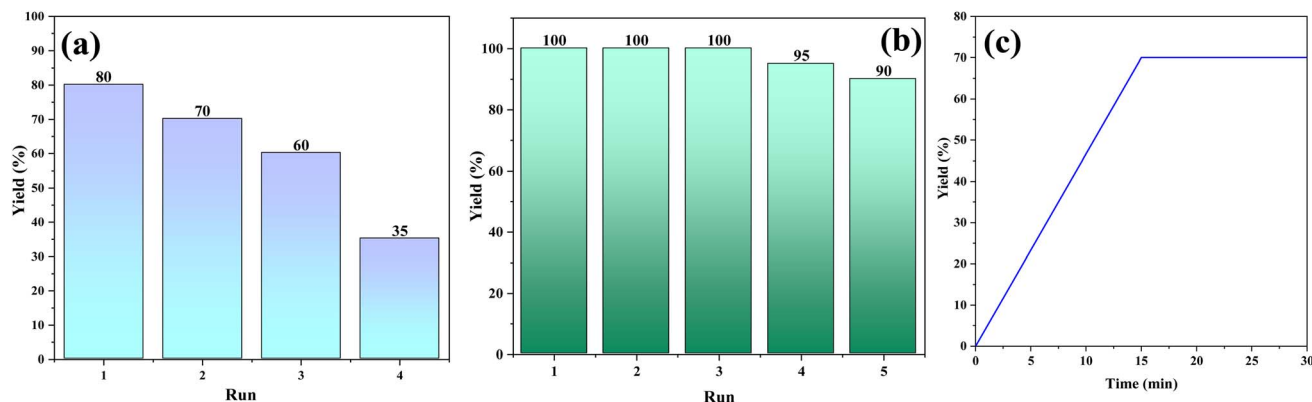


Fig. 6 Recycling experiment in synthesis (a) propargylamines and (b) tetrazoles, and (c) leaching experiment of Cu(OH)<sub>2</sub>-BSH catalyst.

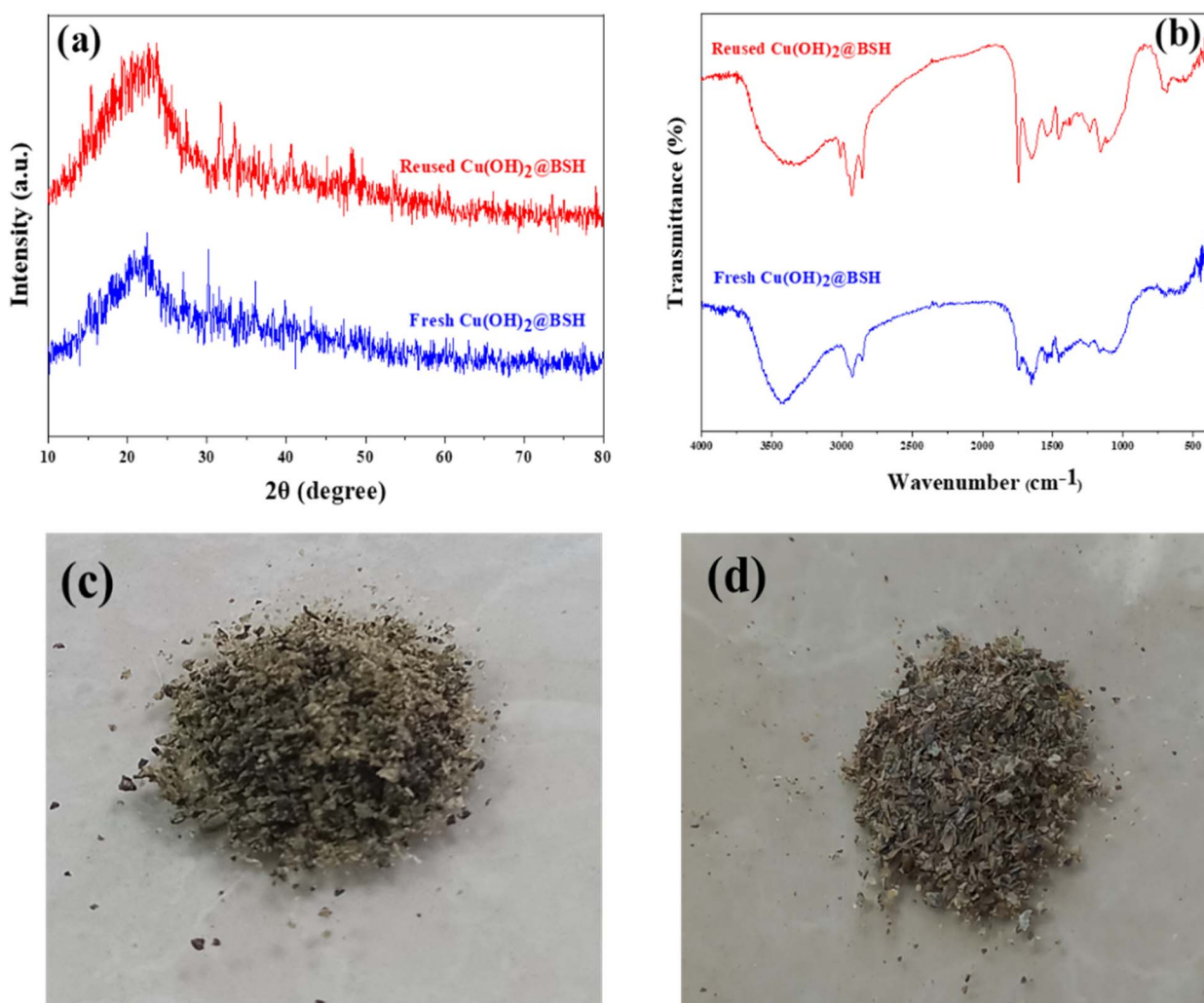


Fig. 7 XRD patterns (a) and FT-IR spectra (b) of Cu(OH)<sub>2</sub>-BSH before and after catalytic process and digital photographs of Cu(OH)<sub>2</sub>-BSH before (c) and after (d) catalytic process.

### 3.7. Economic evaluation

In previous years, multi-component reactions have often utilized larger quantities of copper, sometimes in conjunction with ligands or expensive metals, as catalysts in addition to

copper.<sup>66</sup> Moreover, in scenarios where natural materials were used as substrates for stabilizing copper, not only were substantial amounts of the substrate and copper metal utilized in large-scale production, proving cost-effective (6.2 dollars per



Table 5 Comparison of the Cu(OH)<sub>2</sub>-BSH catalyst's catalytic activity in the production of propargylamine

Entry	Catalyst	Condition	Time (h:min)	Yield (%)	Ref.
1	Cu/HM	Solvent-free, 110 °C	2:00	92	59
2	Cu/Gr	Ar atmosphere, 100 °C	24:00	100	60
3	H-Fe <sub>3</sub> O <sub>4</sub> -h-Cu <sup>0</sup> -mSiO <sub>2</sub>	Solvent-free, 110 °C	00:15	98	57
4	Cu(II)-MOC	N <sub>2</sub> atmosphere, 60 °C	02:00	98	61
5	Cu(OH) <sub>2</sub> -BSH	Solvent-free, 100 °C	00:30	100	This work

Table 6 Comparison of the Cu(OH)<sub>2</sub>-BSH catalyst's catalytic activity in the production of tetrazole

Entry	Catalyst	Condition	Time (h:min)	Yield (%)	Ref.
1	Cu@APS-TDU-PMO	Solvent-free, 110 °C	0:50	97	62
2	Cu(OAc) <sub>2</sub>	DMF, 120 °C	12:00	98	63
3	Cu-MCM-41	DMF, 100 °C	12:00	90	64
4	Fe <sub>3</sub> O <sub>4</sub> -CNT-TEA-Cu(II)	DMF, 70 °C	01:30	96	65
5	Cu(OH) <sub>2</sub> -BSH	DMF, 100 °C	00:05	100	This work

ton), but substantial quantities of the resulting catalyst were also necessary for the reactions.<sup>67</sup> To address these concerns, we endeavored to reduce the cost of catalyst production and enhance its environmental friendliness by using minimal quantities of natural basil seed hydrogel for stabilization as well as the smallest possible amount of copper hydroxide for catalysis, all while achieving efficient performance in multi-component reactions.

## 4. Conclusion

In conclusion, the pharmaceutical industry's consistent demand for propargyl amines and tetrazoles has long presented a substantial challenge. These compounds are crucial, and their synthesis heavily relies on catalysis. Unfortunately, the availability of stable and efficient catalysts has been a limiting factor. To address this pressing issue, we have successfully developed an environmentally friendly and sustainable catalyst, known as Cu(OH)<sub>2</sub>-BSH. This innovative catalyst is created by incorporating copper hydroxide into a basil seed hydrogel matrix, forming a 3D nanoreactor support structure. This comprehensive analysis has not only confirmed the presence of Cu(OH)<sub>2</sub> within the catalyst but has also revealed a porous structure. This porous nature enhances diffusion rates and provides a multitude of active sites, resulting in exceptional effectiveness. The catalyst offers a substantial surface area, can be easily recovered, and represents a cost-effective, safe, and readily available solution. The application of this novel catalyst to the synthesis of propargyl amines and tetrazoles through multi-component reactions has yielded outstanding results under mild conditions and within a remarkably short timeframe. Consequently, this work offers a practical and straightforward approach for designing and synthesizing metal hydroxides and 3D hydrogels, which can be effectively employed in heterogeneous catalysis for organic syntheses. Crucially, this approach can be realized using basic and affordable starting materials at the molecular level, promising significant contributions to sustainable and environmentally responsible catalysis.

## Conflicts of interest

There are no Conflicts of interest.

## References

- 1 F. Movahedi, H. Masrouri and M. Kassaei, *J. Mol. Catal. A: Chem.*, 2014, **395**, 52–57.
- 2 S. Arshadi, E. Vessally, L. Edjlali, R. Hosseinzadeh-Khanmiri and E. Ghorbani-Kalhor, *Beilstein J. Org. Chem.*, 2017, **13**, 625–638.
- 3 K. Lauder, A. Toscani, N. Scalacci and D. Castagnolo, *Chem. Rev.*, 2017, **117**, 14091–14200.
- 4 N. Fischer, K. Karaghiosoff, T. M. Klapötke and J. Stierstorfer, *Z. Anorg. Allg. Chem.*, 2010, **5**, 735–749.
- 5 R. S. Upadhyaya, S. Jain, N. Sinha, N. Kishore, R. Chandra and S. K. Arora, *Eur. J. Med. Chem.*, 2004, **39**, 579–592.
- 6 Y. Li, K. K. Pasunooti, R.-J. Li, W. Liu, S. A. Head, W. Q. Shi and J. O. Liu, *J. Med. Chem.*, 2018, **61**, 11158–11168.
- 7 J. Zhang, S. Wang, Y. Ba and Z. Xu, *Eur. J. Med. Chem.*, 2019, **178**, 341–351.
- 8 S. J. Wittenberger, *Org. Prep. Proced. Int.*, 1994, **26**, 499–531.
- 9 R. S. Varma, *Green Chem.*, 2014, **16**, 2027–2041.
- 10 N. Khaleghi, Z. Mojtahapour, Z. Rashvandi, A. Mohammadi, M. Forouzandeh-Malati, F. Ganjali, S. Zarei-Shokat, A. Kashtiaray, R. Taheri-Ledari and A. Maleki, *Nanoscale Adv.*, 2023, **5**, 4911–4924.
- 11 H. P. Dijkstra, G. P. Van Klink and G. Van Koten, *Acc. Chem. Res.*, 2002, **35**, 798–810.
- 12 U. Chinna Rajesh, U. Gulati and D. S. Rawat, *ACS Sustain. Chem. Eng.*, 2016, **4**, 3409–3419.
- 13 M. Zarei, I. Mohammadzadeh, K. Saidi and H. Sheibani, *ACS Omega*, 2023, **8**, 18685–18694.
- 14 N. Nouruzi, M. Dinari, N. Mokhtari, B. Gholipour, S. Rostammia, S. Khaksar and R. Boluki, *Appl. Organomet. Chem.*, 2020, **34**, e5677.



- 15 J. E. ten Elshof, H. Yuan and P. Gonzalez Rodriguez, *Adv. Energy Mater.*, 2016, **6**, 1600355.
- 16 M. Li, J. Liu, Y. Xu and G. Qian, *Environ. Rev.*, 2016, **24**, 319–332.
- 17 J. F. Souza, G. P. Costa, R. Luque, D. Alves and A. R. Fajardo, *Catal. Sci. Technol.*, 2019, **9**, 136–145.
- 18 C. Parmeggiani, C. Matassini and F. Cardona, *Green Chem.*, 2017, **19**, 2030–2050.
- 19 N. Sahiner, *Prog. Polym. Sci.*, 2013, **38**, 1329–1356.
- 20 Y. Hou, S. Ogasawara, A. Fukuoka and H. Kobayashi, *Catal. Sci. Technol.*, 2017, **7**, 6132–6139.
- 21 S. Zhang, Y.-R. Lee, H.-j. Jeon, W.-S. Ahn and Y.-M. Chung, *Mater. Lett.*, 2018, **215**, 211–213.
- 22 A. Fihri, D. Cha, M. Bouhrara, N. Almaná and V. Polshettiwar, *ChemSusChem*, 2012, **5**, 85–89.
- 23 S. E. García-Garrido, J. Francos, V. Cadierno, J. M. Basset and V. Polshettiwar, *ChemSusChem*, 2011, **4**, 104–111.
- 24 N. Madhavan, C. W. Jones and M. Weck, *Acc. Chem. Res.*, 2008, **41**, 1153–1165.
- 25 A. Schätz, R. N. Grass, W. J. Stark and O. Reiser, *Chem. Eur. J.*, 2008, **14**, 8262–8266.
- 26 E. Guibal, *Prog. Polym. Sci.*, 2005, **30**, 71–109.
- 27 M. Tukhani, F. Panahi and A. Khalafi-Nezhad, *ACS Sustain. Chem. Eng.*, 2018, **6**, 1456–1467.
- 28 Z. Xiang, Y. Chen, Q. Liu and F. Lu, *Green Chem.*, 2018, **20**, 1085–1094.
- 29 E. M. Ahmed, *J. Adv. Res.*, 2015, **6**, 105–121.
- 30 G. Fu, Y. Chen, Z. Cui, Y. Li, W. Zhou, S. Xin, Y. Tang and J. B. Goodenough, *Nano Lett.*, 2016, **16**, 6516–6522.
- 31 A. K. Gaharwar, N. A. Peppas and A. Khademhosseini, *Biotechnol. Bioeng.*, 2014, **111**, 441–453.
- 32 D. Seliktar, *Science*, 2012, **336**, 1124–1128.
- 33 G. Fu, X. Yan, Y. Chen, L. Xu, D. Sun, J. M. Lee and Y. Tang, *Adv. Mater.*, 2018, **30**, 1704609.
- 34 Y. Shi, J. Zhang, L. Pan, Y. Shi and G. Yu, *Nano Today*, 2016, **11**, 738–762.
- 35 J. Anjali, V. K. Jose and J.-M. Lee, *J. Mater. Chem.*, 2019, **7**, 15491–15518.
- 36 P. Thoniyot, M. J. Tan, A. A. Karim, D. J. Young and X. J. Loh, *Adv. Sci.*, 2015, **2**, 1400010.
- 37 S. Bashir, M. Hina, J. Iqbal, A. Rajpar, M. Mujtaba, N. Alghamdi, S. Wageh, K. Ramesh and S. Ramesh, *Polymers*, 2020, **12**, 2702.
- 38 X. Zhu, Y. Chen, R. Xie, H. Zhong, W. Zhao, Y. Liu and H. Yang, *Front. Chem.*, 2021, **9**, 794755.
- 39 X. Wen, W. Zhang and S. Yang, *Langmuir*, 2003, **19**, 5898–5903.
- 40 H. H. Gahrue, M. H. Eskandari, P. Van der Meer and S. M. H. Hosseini, *Carbohydr. Polym.*, 2019, **219**, 155–161.
- 41 F. V. Cabral, B. d. M. Santana, C. N. Lange, B. L. Batista, A. B. Seabra and M. S. Ribeiro, *Pharmaceutics*, 2023, **15**, 1971.
- 42 J. Kang, S. W. Cui, J. Chen, G. O. Phillips, Y. Wu and Q. Wang, *Food Hydrocolloids*, 2011, **25**, 1984–1990.
- 43 H. Mittal, A. Maity and S. Sinha Ray, *J. Phys. Chem. B*, 2015, **119**, 2026–2039.
- 44 J. Li, X. Kong, M. Jiang and X. Lei, *J. Mater. Sci.*, 2018, **53**, 16263–16275.
- 45 J. Wang, L. Zhu, L. Ji and Z. Chen, *J. Mater. Sci.*, 2018, **33**, 581–589.
- 46 R. Singh, D. Pal and S. Chattopadhyay, *ACS Omega*, 2020, **5**, 21768–21780.
- 47 M. Amiri, K. Dashtian, M. Ghaedi and S. Mosleh, *Photochem. Photobiol. Sci.*, 2020, **19**, 943–955.
- 48 S. Mosleh, M. R. Rahimi, M. Ghaedi, K. Dashtian and S. Hajati, *Ultrason. Sonochem.*, 2018, **40**, 601–610.
- 49 S. Parsaei, M. Rashid, A. Ghoorchian, K. Dashtian and D. Mowla, *J. Chem. Eng.*, 2023, **475**, 146448.
- 50 R. Vasquez, *Surf. Sci. Spectra*, 1998, **5**, 267–272.
- 51 R. Vasquez, *Surf. Sci. Spectra*, 1998, **5**, 257–261.
- 52 R. Vasquez, *Surf. Sci. Spectra*, 1998, **5**, 262–266.
- 53 W. Zhang, X. Wen, S. Yang, Y. Berta and Z. L. Wang, *Adv. Mater.*, 2003, **15**, 822–825.
- 54 S. D. Bhagat, Y.-H. Kim, K.-H. Suh, Y.-S. Ahn, J.-G. Yeo and J.-H. Han, *Microporous Mesoporous Mater.*, 2008, **112**, 504–509.
- 55 B. Arunraj, T. Sathvika, V. Rajesh and N. Rajesh, *ACS Omega*, 2019, **4**, 940–952.
- 56 Z. Ye, F. Wang, Y. Li and F. Zhang, *Green Chem.*, 2018, **20**, 5271–5275.
- 57 Z. Elahimehr, F. Nemati and A. Elhampour, *Arab. J. Chem.*, 2020, **13**, 3372–3382.
- 58 J. Bi, Y. Dong, D. Meng, D. Zhu and T. Li, *Polymer*, 2019, **164**, 183–190.
- 59 U. Chinna Rajesh, U. Gulati and D. S. Rawat, *ACS Sustain. Chem. Eng.*, 2016, **4**, 3409–3419.
- 60 S. Frindy, A. El Kadib, M. Lahcini, A. Primo and H. Garcia, *Catal. Sci. Technol.*, 2016, **6**, 4306–4317.
- 61 G.-J. Chen, C.-Q. Chen, X.-T. Li, H.-C. Ma and Y.-B. Dong, *Chem. Commun.*, 2018, **54**, 11550–11553.
- 62 E. Valiey and M. G. Dekamin, *Sci. Rep.*, 2022, **12**, 18139.
- 63 U. B. Patil, K. R. Kumthekar and J. M. Nagarkar, *Tetrahedron Lett.*, 2012, **53**, 3706–3709.
- 64 M. Abdollahi-Alibeik and A. Moaddeli, *New J. Chem.*, 2015, **39**, 2116–2122.
- 65 P. Akbarzadeh, N. Koukabi and E. Kolvari, *Mol. Divers.*, 2020, **24**, 319–333.
- 66 S. Nakamura, M. Ohara, Y. Nakamura, N. Shibata and T. Toru, *Chem.–Eur. J.*, 2010, **16**, 2360–2362.
- 67 M. Gholinejad, F. Saadati, S. Shaybanizadeh and B. Pullithadathil, *RSC Adv.*, 2016, **6**, 4983–4991.

